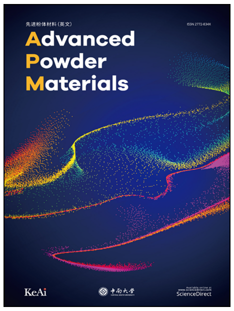

Coupled Polymer-Cation Coordination and Anion-Derived Inorganic-Rich Interphases in Ionic Liquid-Regulated Gel Electrolytes for Stable Lithium Metal Batteries

Jiaying Chen, Kaizhen Li, Ruohan Hou, Shijie Zhang, Guosheng Shao, Peng Zhang

PII: S2772-834X(26)00053-9

DOI: https://doi.org/10.1016/j.apmate.2026.100445

Reference: APMATE 100445

To appear in: *Advanced Powder Materials*

Received Date: 2 April 2026

Revised Date: 21 June 2026

Accepted Date: 22 June 2026

Please cite this article as: J. Chen, K. Li, R. Hou, S. Zhang, G. Shao, P. Zhang, Coupled Polymer-Cation Coordination and Anion-Derived Inorganic-Rich Interphases in Ionic Liquid-Regulated Gel Electrolytes for Stable Lithium Metal Batteries, *Advanced Powder Materials*, https://doi.org/10.1016/j.apmate.2026.100445.

Coupled Polymer-Cation Coordination and Anion-Derived Inorganic-Rich Interphases in Ionic Liquid-Regulated Gel Electrolytes for Stable Lithium Metal Batteries

Jiaying Chen[a,b,1], Kaizhen Li[a,b,1,], Ruohan Hou[a,b,1,*], Shijie Zhang[a,b], Guosheng Shao[a,b,**], Peng Zhang[a,b,***]

[a] State Center for International Cooperation on Designer Low-carbon & Environmental Materials (CDLCEM), School of Materials Science and Engineering, 100 Kexue Avenue, Zhengzhou University, Zhengzhou 450001, China Institution
[b] Zhengzhou Materials Genome Institute (ZMGI), Xingyang, Zhengzhou 450100, China.
* Corresponding author.
E-mail addresses: hourh@zzu.edu.cn (R.H. Hou), gsshao@zzu.edu.cn (G.S. Shao), zhangp@zzu.edu.cn (P. Zhang).
[1] These authors contributed equally to this work.

Jiaying Chen is currently pursuing her master degree under the supervision of Prof. Guosheng Shao and Prof. Peng Zhang in School of Materials Science and Engineering, Zhengzhou University. Her research focuses on the design of composite polymer electrolytes and the study and application of their performance in lithium metal batteries.

RuohanHou received his Ph.D. degree in the School of Materials Science and Engineering from Zhengzhou University (2025). Then, he joined the School of Materials Science and Engineering at Zhengzhou University as a direct-appointed associate professor in 2025.His currentresearch interests focus on the development of high-entropy nanomaterials, the design of functionalized composite electrode structures for Li-S batteries, and the exploration of catalyst mechanisms inreal-time electrochemical processes.

Guosheng Shao is the founding director of the State Centre for International Cooperation on Designer Low-carbon and Environmental Materials (CDLCEM) at Zhengzhou University, China. He is also the founding director of the Zhengzhou Materials Genome Institute (ZMGI, 2016-) and a Visiting Professor at the University of Surrey, UK (2018-). He earned his Ph.D. in materials science at the Universityof Surrey and then worked across UK universities as a senior academic member. His current focus is on sustainable (renewable) energy systems and environmental materials technologies. He serves as Editor-in-Chief of Energy & Environmental Materials.

Peng Zhang received his Ph.D. in Materials Physical and Chemistry from Northeast Normal University, China (2014). After postdoctoral research at Helmholtz-Zentrum Berlin, Germany, he joined the School of Materials Science and Engineering at Zhengzhou University as a full professor (2016). His current research interests focus on low-dimensional carbon-based materials and their applications in the fields of environment remediation and energy storage. He serves on the editorial boards/young advisory boards of Scientific Report, InfoMat, Energy & Environmental Materials, etc.

Acknowledgements

The work was supported by the National Natural Science Foundation of China (No. 52472110, U2004172, 51972287), the Central Plains Science and Technology Innovation Leading Talents (254000510052), the National Natural Science Foundation of Henan Province (No. 242300421008), and the Program for Science& Technology Innovation Talents in Universities of Henan Province (23HASTIT001).

Graphical Abstract

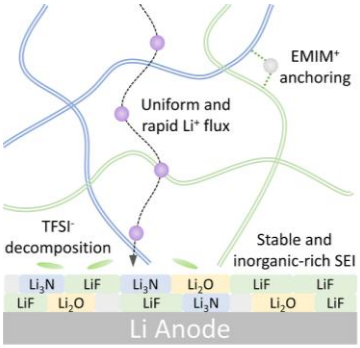

A coupled regulation strategy is proposed to stabilize electrolyte-electrodel interface by integrating polymer-cation coordination with anion-driven interfacial reactions in a gel polymer electrolyte. Preferential polymer-cation interactions ensure fast and uniform Li$^+$ flux, while anion-derived reactions induce an inorganic-rich SEI, enabling dendrite-free lithium deposition and long-term cycling stability across multiple battery configurations.

Coupled Polymer-Cation Coordination and Anion-Derived Inorganic-Rich Interphases in Ionic Liquid-Regulated Gel Electrolytes for Stable Lithium Metal Batteries

Abstract: The practical application of lithium metal batteries is constrained by low coulombic efficiency and safety risks arising from Li dendrite growth. Developing functional gel polymer electrolytes (GPEs) systems is recognized as promising approach to address these challenges. In this work, a novel GPE (HFP/PEO-EMIM) was obtained by functionalizing the PVDF-HFP/PEO composite with EMIMTFSI ionic liquid. The resulting HFP/PEO-EMIM exhibits strong chemical stability and excellent heat resistance. The introduction of EMIMTFSI improves the interfacial compatibility between HFP/PEO-EMIM and the Li anode. More importantly, experiments and theoretical calculations show that $EMIM^+$ cations preferentially interact with polymer molecules, ensuring high Li flux and accelerating its transport. Therefore, HFP/PEO-EMIM exhibits a high ionic conductivity of 1.82 mS cm^{-1}. Additionally, the enriched $TFSI^-$ promotes the formation of a stable inorganic-rich SEI, enabling uniform Li deposition. As expected, the Li||HFP/PEO-EMIM||Li symmetric cell maintains low voltage hysteresis after stable cycling for 3600 h, and the optimized $LiFePO_4$||Li full cell retains 95% of its initial capacity after 650 cycles at 1 C, remaining stable for over 500 cycles at 3 C. Furthermore, extended cycle life was also observed in $LiCoO_2$ cells and $LiFePO_4$ pouch cells, underscoring the broad practical potential of the proposed electrolyte system.

Keywords: Gel electrolyte; Ionic liquid; Solid electrolyte interphase; Ion transport; Lithium metal battery.

1. Introduction

Lithium metal batteries (LMBs) are widely regarded as next-generation energy-storage systems due to the exceptionally high theoretical capacity (3860 mAh g^{-1}) and ultralow redox potential (−3.04 V vs. SHE) of lithium (Li) metal anodes [1,2]. During the operation of LMBs, the inherently high redox activity of Li metal leads to side reactions with conventional liquid electrolytes, resulting in the formation of a solid electrolyte interphase (SEI) layer on the Li anode surface [3,4]. Due to differences in chemical composition, this SEI is typically unstable in most electrolyte systems, repeatedly breaking down and remodeling during electrochemical cycling [5,6]. This instability leads to continuous electrolyte consumption and promotes Li dendrite growth, resulting in rapid capacity decay and reduced coulombic efficiency [7]. Furthermore, the poor thermal stability of commercially available separators increases the risk of short circuits and thermal runaway, significantly hindering the commercialization of LMBs [8]. Fundamentally, these challenges originate from the insufficient regulation of Li^+ transport and interphase chemistry at the electrolyte/Li anode interface.

To address these issues, extensive research efforts have been conducted, including the design of lithiophilic hosts, optimization of artificial interface engineering, functionalized electrolyte additives, and the development of diverse alternative electrolyte systems etc. [9-12]. Among these, gel polymer electrolytes (GPEs) are considered as promising alternatives to liquid electrolytes due to their chemical stability, flame retardancy, favorable mechanical flexibility, and compatibility with established cell fabrication processes. In GPEs, liquid components are confined within polymer matrices, thereby enhancing safety, improving electrolyte utilization, and accelerating ion transport [13,14]. Recently, GPEs systems based on polymers such as poly vinylidene fluoride (PVDF), poly ethylene oxide (PEO), and polyacrylonitrile (PAN) have made significant progress and have proven effective in enhancing the electrochemical performance of LMBs [15-17]. Nevertheless, single-polymer-based GPEs often suffer from intrinsic trade-offs between ionic conductivity, mechanical strength, and thermal stability, making it difficult to meet the multifaceted requirements of advanced LMBs [18]. For instance, PEO offers good ionic conductivity but has relatively weak mechanical strength and poor high-temperature stability [19]. In contrast, polymers like PVDF provide excellent thermal stability and mechanical strength but suffer from low ionic conductivity [20]. Therefore, overcoming the limitations of single polymer systems may be achievable by combining the properties of different polymers and polymerizing them at the molecular level to construct multi-polymer based GPEs.

Although combining multiple polymers can partially alleviate these limitations by integrating complementary properties, interfacial instability with Li metal remains a persistent challenge. Additionally, due to poor interfacial compatibility between GPEs and the Li metal anode, the physical inhibition provided by GPEs alone is insufficient to effectively suppress dendrite growth over long cycles, thus exacerbating interfacial issues and diminishing the electrochemical performance of LMBs. To address the issue of poor interface compatibility between GPEs and Li anode, a wide range of strategies has been explored, including ceramic filler reinforcement, polymer functionalization, and artificial interlayer construction design [21-23]. While these approaches have each contributed to incremental improvements, they also exhibit inherent limitations. Ceramic fillers in GPEs tend to agglomerate, causing localized ion transport difficulties and potentially leading to interfacial delamination from polymers due to volume changes [24]. Functionalized polymer backbones or side chains may undergo chain breakage, oxidation, or reductive degradation after prolonged cycling, leading to diminished mechanical properties and reduced ionic conductivity [25]. Artificial interlayers increase fabrication complexity and pose a risk of peeling over time [26]. More critically, most existing GPE designs primarily focus on macroscopic mechanical reinforcement or physical confinement, while overlooking the molecular-level coordination between Li^+, polymer chains, and counter ions, which fundamentally governs both ion transport behavior and interfacial reactions. These limitations highlight the necessity of a more fundamental strategy that directly regulates ion-polymer coordination and interphase chemistry at the molecular level, rather than relying solely on physical or structural modifications.

Ionic liquids (ILs), defined as molten salts composed of organic cations and inorganic/organic anions [27]. They are characterized by properties such as low volatility, excellent electrochemical stability, and a wide electrochemical window, making them highly suitable for applications in areas like electrolytes, energy catalysis and other fields. Recent advances in IL applications for LMBs include imidazole-based, pyrrolidinium-based, and quaternary ammonium-based electrolyte systems, which demonstrate superior electrochemical performance [28-31]. Thanks to their ability to regulate Li deposition kinetics, excellent interfacial compatibility, and enhanced mechanical barrier properties, ILs offer multifunctional advantages in effectively suppressing Li dendrite growth [32]. For example, Li et al. [33] designed zwitterionic bottlebrush polymer electrolytes incorporating $Pyr_{13}TFSI$, which regulate Li^+ transport and interfacial chemistry, enhance ionic conductivity, and enable long-cycling, stable quasi-solid-state lithium metal batteries. Such promising characteristics have prompted a variety of studies to integrate ILs into advanced GPE systems for further performance optimization. Among the diverse ILs investigated, EMIMTFSI stands out due to several key advantages over alternatives such as $PYR_{14}TFSI$, EMIMFSI, or $EMIMBF_4$. $EMIM^+$ cation possesses a delocalized charge distribution and $TFSI^-$ anion exhibits superior stability, lower lattice energy, and stronger Li^+ coordination capability compared to FSI^- or BF_4^- [34,35]. These enable the formation of localized high-concentration Li^+ microenvironments and promoting favorable anion-derived SEI formation [36]. EMIMTFSI also displays a wide electrochemical stability window and low viscosity among imidazolium-based ILs [37]. These combined features offer a molecularly tunable platform for modulating ion transport and interfacial reactions, which capabilities that many alternative IL systems lack. Therefore, chemically stable composite GPEs with high ionic conductivity can be achieved through the synergistic integration of EMIMTFSI within a multi-polymer framework, where the combined polymer architecture and IL jointly regulate interfacial interactions. This cooperative design enables balanced Li^+ coordination and promotes a more homogeneous Li^+ distribution throughout the electrolyte. Simultaneously, the same synergistic environment facilitates the formation of a uniform, inorganic-rich SEI at the Li metal interface, thereby enhancing interfacial stability. Consequently, the electrochemical performance and cycling durability of LMBs are substantially improved.

Herein, based on the density functional theory simulations, we present a GPE system (HFP/PEO-EMIE) that uses EMIMTFSI IL to modify PVDF-HFP/PEO composite polymers as an alternative to the liquid electrolyte in LMBs. The PVDF-HFP/PEO polymer freestanding film was fabricated via electrospinning, ensuring uniform polymer molecules entanglement, while EMIMTFSI is confined within the porous structure of interwoven nanofibers, effectively preventing phase separation.

Fundamentally, PVDF-HFP offers a mechanically robust and thermally stable framework, while PEO enhances Li^+ coordination and reduces polymer crystallinity. Furthermore, the synergistic effect of the hydrophobicity of PVDF-HFP and the ether functional groups of PEO enhances the interfacial compatibility between the electrolyte and electrode. Additionally, EMIMTFSI exhibits excellent compatibility with the PVDF-HFP/PEO matrix, significantly enhancing the intrinsic ionic conductivity (1.82 mS cm^{-1}) of HFP/PEO-EMIE. Experimental and theoretical calculations show that $EMIM^+$ possesses strong affinity toward polymer segments, allowing it to effectively occupy polymer adsorption sites and weaken polymer-Li^+ coordination more efficiently than bulkier pyrrolidinium or ammonium cations. Meanwhile, $TFSI^-$ anions are locally enriched at the anode side and participate in interfacial reactions that induce the formation of inorganic-rich (LiF, Li_3N, and Li_2O) SEI and effectively suppress Li dendrite growth. As a result, Li||HFP/PEO-EMIM||Li symmetric cells demonstrated over 3600 hours of stable cycling, and $LiFePO_4$/$LiCoO_2$ full cells with HFP/PEO-EMIM exhibit excellent electrochemical capacities at high current densities. This work presents a feasible, efficient, and valuable strategy for designing and developing GPEs for next-generation high-performance LMBs.

2. Results and Discussion

2.1 Design and mechanism analysis of HFP/PEO-EMIM GPE

As illustrated in **Fig. 1a** and **Fig. S1**, unlike polypropylene (PP) separator, whose elongated, flat microporous structure and uneven pore size distribution hinder Li^+ migration, coupled with low surface energy and poor wettability leading to uneven Li deposition and dendrite growth, HFP/PEO composite membranes featured a three-dimensional (3D) porous structure. To prepare this membrane, a homogeneous polymer solution consisting of PVDF-HFP and PEO was first fabricated and subsequently processed into a self-supporting HFP/PEO fibrous membrane via electrospinning. The resulting membrane effectively promoted rapid Li^+ migration. However, the narrow electrochemical window and poor interface stability with lithium metal anodes in HFP/PEO composite membranes compromised battery cycle life. Therefore, the electrospun HFP/PEO membrane was further soaked in EMIMTFSI, enabling the in-situ incorporation of $EMIM^+$ cations and $TFSI^-$ anions within the polymer matrix and forming a composite gel polymer electrolyte (HFP/PEO-EMIM). PVDF-HFP, with its high mechanical strength, served as the backbone of the electrolyte. The incorporation of PEO formed a continuous 3D ionic conduction network, enhancing ion transport. Meanwhile, EMIMTFSI interacted with HFP/PEO via hydrogen bonds. Its bulky organic cation $EMIM^+$ effectively inserted between polymer chains, disrupting crystalline structures and increasing the amorphous content, thereby creating more pathways for Li^+ migration.

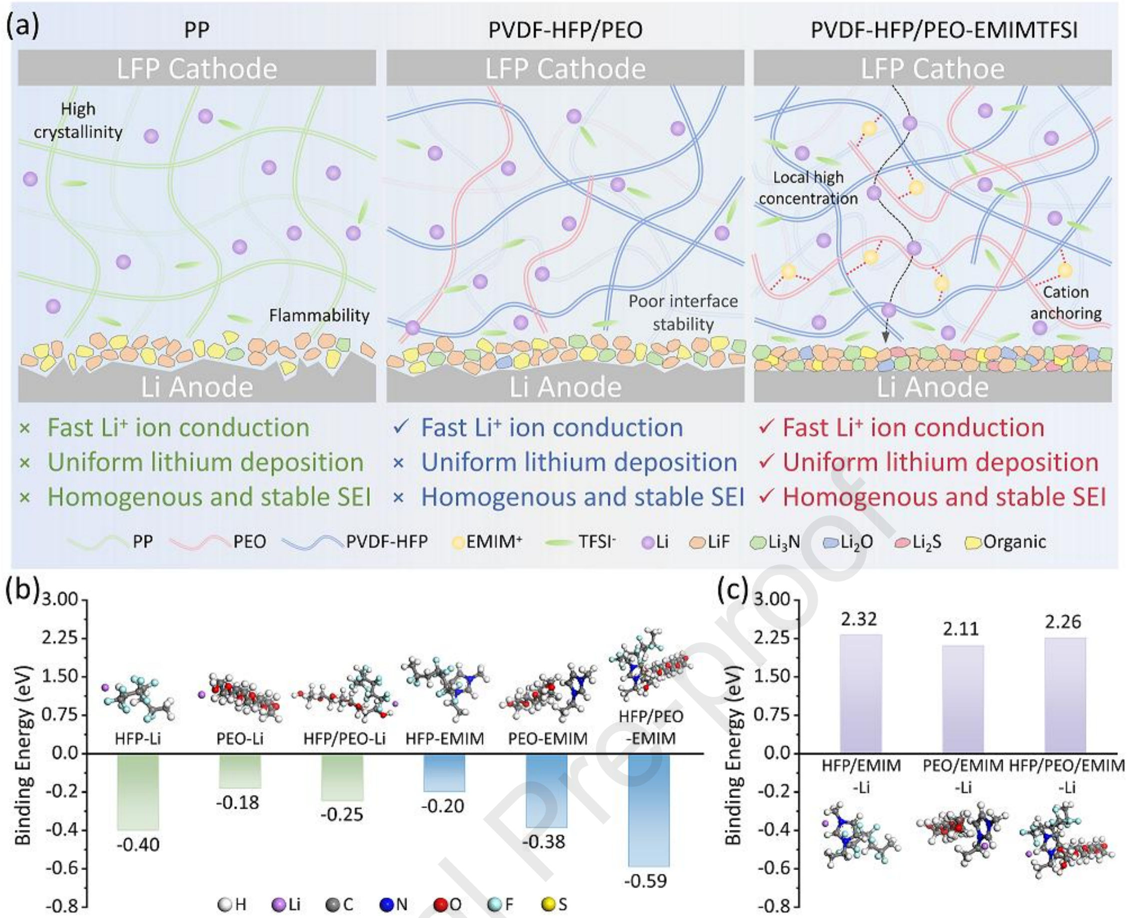

Fig. 1. (a) Schematic of the logic for designing HFP/PEO-EMIM gel polymer electrolyte. (b) Binding energies of various polymers with ions. (c) Binding energies of Li^+ with polymer-EMIM.

The ion-regulation mechanism of the hybrid polymer electrolyte was governed by the distinct binding hierarchies of Li^+ and $EMIM^+$ within the HFP/PEO matrix, as revealed by DFT calculations in **Fig. 1b**. Li^+ exhibited an intermediate binding strength with HFP/PEO (−0.25 eV), lying between those of PVDF-HFP (−0.40 eV) and PEO (−0.18 eV), which provided a balanced coordination environment that stabilizes Li^+ while avoiding excessive immobilization. In contrast, $EMIM^+$ showed a markedly stronger affinity toward the hybrid polymer framework (−0.59 eV) than toward PVDF-HFP (−0.20 eV) or PEO (−0.38 eV), leading to preferential occupation of polymer coordination sites and competitive weakening of Li^+-polymer interactions. Consequently, a portion of Li^+ was released from strong polymer binding, resulting in enhanced Li^+ mobility and improved ionic conductivity. Notably, in **Fig. 1c**, the interaction energy between $EMIM^+$ and Li^+ in the HFP/PEO system is 2.26 eV, further demonstrating that $EMIM^+$ promoted the dissociation of Li^+ from ion clusters and enabled more uniform transport of Li^+ within the electrolyte. As showed in **Fig. S2**, the HFP/PEO matrix displayed higher binding energy toward $TFSI^-$ anions (0.78 eV) compared with PVDF-HFP (0.21 eV) and PEO (0.24 eV). Such strong anion-polymer interaction favored the formation of localized $TFSI^-$-concentration regions. The resulting anion-rich interfacial environment promoted preferential $TFSI^-$ decomposition on the Li metal surface, inducing an inorganic-rich SEI that homogenizes Li^+ flux, suppresses dendritic growth, and enhances interfacial stability and cycling performance, thereby improving battery cycle stability.

2.2 Structure and physical properties

The phase composition of the prepared gel electrolyte was characterized. The surface morphologies of commercial PP, PVDF-HFP, HFP/PEO, and HFP/PEO-EMIM membranes were examined by SEM. PP exhibited large pore diameters and highly aligned fibrous features (**Fig. S3**). In contrast, PVDF-HFP displayed a loose porous morphology with non-uniform fiber thickness (**Fig. 2a**), which may lead to localized high ionic flux and the preferential growth of Li dendrites. The HFP/PEO membrane showed a uniform fiber diameter and interconnected 3D porous structure, which was preserved in the HFP/PEO-EMIM film (**Fig. 2b-c**). Notably, infiltration of EMIMTFSI into this porous network was clearly observed, indicating the formation of continuous Li^+ transport pathways.

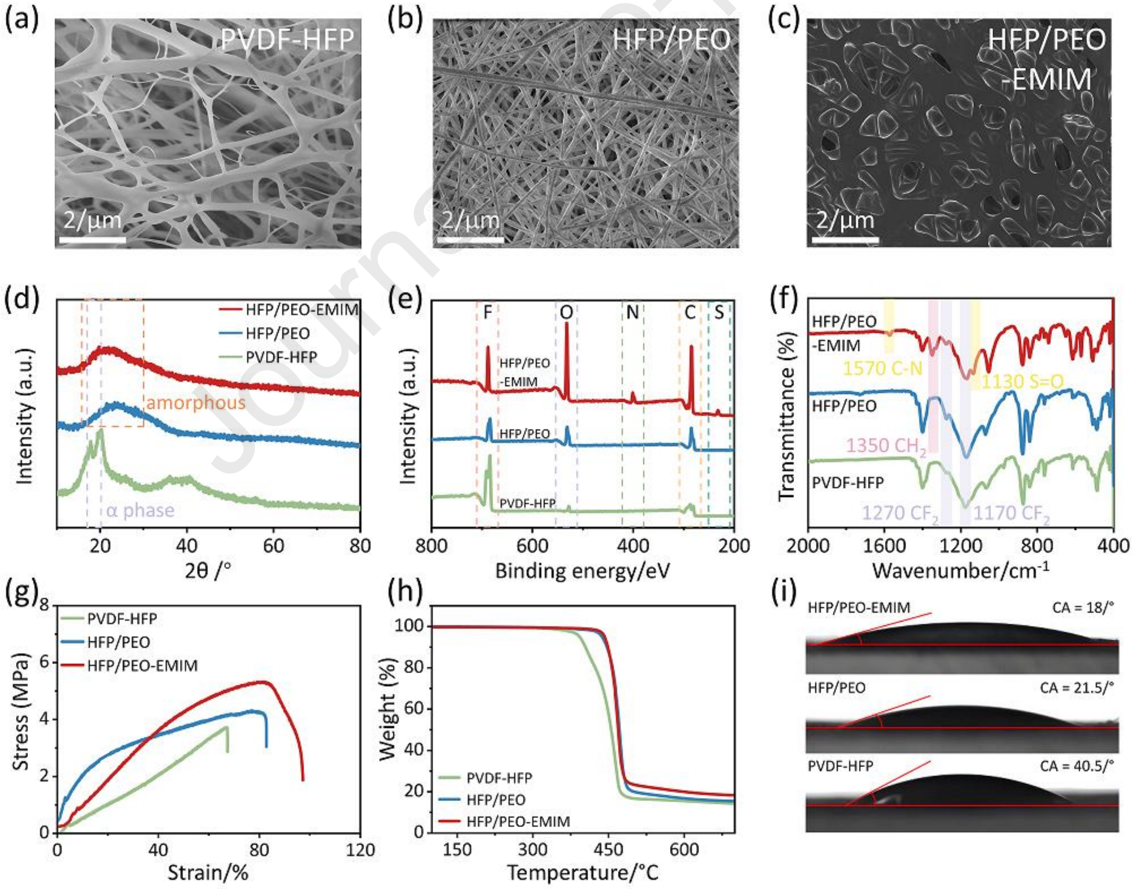

Fig. 2. (a-c) SEM images of PVDF-HFP, HFP/PEO, and HFP/PEO-EMIM. (d) XRD patterns. (e) XPS spectra. (f) FTIR spectra. (g) Stress-strain curves. (h) TGA curves. (i) Contact angle measurements.

The crystalline structure of the GPEs was characterized by XRD (**Fig. 2d**, **Fig. S4**). PP showed sharp diffraction peaks at 14.1° and 17°, corresponding to its α-phase structure, indicative of high crystallinity, which restricts ion transport. PVDF-HFP exhibited diffraction peaks at 17.8° and 20.3°, representing the α- and β-phases of PVDF, respectively. Upon incorporation of PEO and EMIMTFSI, the diffraction pattern of HFP/PEO-EMIM showed a broad peak at 22°, reflecting reduced crystallinity and enhanced amorphous content, which are favorable for ionic mobility. XPS was performed to confirm the surface chemical composition of PVDF-HFP, HFP/PEO and HFP/PEO-EMIM (**Fig. 2e**, **Fig. S5**). The appearance of prominent O 1s peaks at 532 eV in HFP/PEO and HFP/PEO-EMIM indicated PEO integration. The presence of N 1s and S 2p peaks at 400.99 eV and 231.99 eV in HFP/PEO-EMIM confirmed successful EMIMTFSI uptake. Slight oxygen signals in PP and PVDF-HFP samples may arise from residual oxygen during testing. FTIR was used to investigate chemical bonding and functional group interactions. Characteristic C-H stretching and bending bands at 2920, 1454, and 1376 cm^{-1} were observed in PP (**Fig. S6**). As shown in **Fig. 2f**, PVDF-HFP exhibited symmetric and asymmetric $–CF_2–$ stretching vibrations at 1170 and 1270 cm^{-1}, respectively. Peaks assigned to PEO appeared at 1350 cm^{-1} ($–CH_2–$ bending) and 1075 cm^{-1} (C–O–C stretching). Furthermore, imidazole ring vibrations at 1570 cm^{-1} and S=O symmetric stretching at 1130 cm^{-1} further confirmed the successful incorporation of EMIMTFSI. Notably, the C–O–C stretching band of PEO in HFP/PEO appeared at 1075 cm^{-1}. Upon incorporation of EMIMTFSI, this peak shifted to 1053 cm^{-1} (**Fig. S7**), indicating hydrogen-bonding interactions between EMIM$^+$ cations and ether oxygens that weaken the C–O bond. This suggested that EMIM$^+$ interacts with ether oxygens and may partially alter Li$^+$-polymer coordination environments. As shown in **Fig. S8a-b**, MD simulation configurations revealed that HFP/PEO-EMIM formed a more compact and ion-rich environment than HFP/PEO. RDF analysis of Li–O (TFSI$^-$) showed a higher first-shell peak for HFP/PEO-EMIM, indicating increased TFSI$^-$ coordination with Li$^+$ (**Fig. S8c**). Furthermore, Raman spectra (**Fig. S8d**) indicated that HFP/PEO contained mainly free TFSI$^-$, whereas HFP/PEO-EMIM exhibited a higher coordinated fraction (43%), suggesting enhanced anion participation in the Li$^+$ solvation sheath.

To address safety concerns under prolonged cycling and elevated temperatures, the mechanical strength and flame retardancy of the HFP/PEO-EMIM GPE were systematically evaluated. As shown in **Fig. 2g** and **Fig. S9**, the stress-strain curves revealed that HFP/PEO-EMIM exhibited the highest tensile strength (5.29 MPa) compared to PP (2.21 MPa), PVDF-HFP (3.68 MPa), and HFP/PEO (4.22 MPa). This enhancement is attributed to the incorporation of PEO and EMIMTFSI, which reduce the crystallinity of PVDF-HFP and reinforce the polymer network. The improved mechanical robustness of HFP/PEO-EMIM implies enhanced resistance against potential Li dendrite penetration. Flame retardancy was assessed via direct flame exposure tests (**Fig. S10**). While PP, PVDF-HFP, and HFP/PEO membranes rapidly shrank and ignited upon flame contact, the HFP/PEO-EMIM membrane exhibited no visible ignition or deformation. Among them, HFP/PEO-EMIM demonstrated the highest fire resistance, owing to the synergistic effect between the thermally stable polymer framework and the intrinsic flame-retardant nature of EMIMTFSI. Notably, HFP/PEO-EMIM maintained its structural integrity after flame exposure and cooling, which is crucial for preventing internal short circuits during thermal runaway. Thermal stability was further analyzed via thermogravimetric analysis (TGA) (**Fig. 2h**, **Fig. S11**). The onset of mass loss for PP occurred around 300 °C, whereas PVDF-HFP, HFP/PEO, and HFP/PEO-EMIM showed delayed decomposition at higher temperatures, confirming the superior thermal resistance of the composite GPEs.

Porosity and surface area characteristics of the various films were evaluated by nitrogen adsorption-desorption isotherms (**Fig. S12**). The BET specific surface areas of PP, PVDF-HFP, HFP/PEO, and HFP/PEO-EMIM were 26.26 m^2 g^{-1}, 1.62 m^2 g^{-1}, 2.21 m^2 g^{-1}, and 2.06 m^2 g^{-1}, respectively. While a certain degree of porosity benefits Li^+ transport, excessive specific surface area-as in PP-can hinder electrolyte infiltration and promote undesirable electrolyte decomposition, leading to an organic-rich SEI. In contrast, PVDF-HFP, HFP/PEO, and HFP/PEO-EMIM exhibited moderate surface areas suitable for electrolyte retention and Li^+ transport. Among them, HFP/PEO-EMIM had the highest surface area, promoting more uniform Li^+ flux. Pore structure analysis revealed that PP contained micropores, mesopores, and macropores, whereas PVDF/HFP primarily consisted of micropores and macropores. HFP/PEO and HFP/PEO-EMIM, in comparison, exhibited predominantly microporous and mesoporous structures. Such distributions effectively confine EMIMTFSI within the polymer network and suppress phase separation. Moreover, HFP/PEO-EMIM showed a higher cumulative pore volume (0.47 cm^3 g^{-1}) and more suitable pore size distribution compared to PVDF-HFP and HFP/PEO, indicating an optimized porous architecture conducive to Li^+ transport and electrolyte stability. Interfacial wettability was investigated through contact angle measurements and electrolyte uptake tests (**Fig. 2i**, **Fig. S13-S14**). HFP/PEO-EMIM exhibited the lowest contact angle (18°), compared to PP (51°), PVDF-HFP (40.5°), HFP-EMIM (29°) and HFP/PEO (21.5°), indicating enhanced electrolyte affinity resulting from the presence of polar functional groups in PEO and EMIMTFSI. Although HFP/PEO-EMIM showed slightly lower electrolyte uptake (551%) compared to HFP/PEO (657%), due to partial pore occupation by the ionic liquid, it still significantly outperformed PP (282%) and PVDF-HFP (399%). The high uptake capability minimizes electrolyte leakage risk. Furthermore, after a 2-hour rest, HFP/PEO-EMIM retained 286% of absorbed electrolyte, higher than PVDF-HFP (196%) and PP (150%), and only slightly lower than HFP/PEO (335%). This strong electrolyte retention ability promotes stable Li^+ transport. The superior interfacial compatibility of HFP/PEO-EMIM facilitates uniform Li^+ flux across the electrode surface, leading to homogeneous Li deposition and effective suppression of dendrite formation.

2.3 Electrochemical properties and reaction kinetics

Building on the favorable structural and physicochemical characteristics of HFP/PEO-EMIM, its electrochemical properties were systematically evaluated to further validate its applicability in high-performance LMBs. To confirm that the performance enhancement arises from polymer/IL synergy rather than mere liquid electrolyte uptake, a control sample HFP-EMIM (PVDF-HFP membrane without PEO soaked in the identical EMIMTFSI/electrolyte mixture) was prepared. As evidenced in **Fig. 3a** and **Fig. S15**, the ionic conductivity of HFP/PEO-EMIM reached 1.82 mS cm^{-1}, significantly higher than that of PP (0.59 mS cm^{-1}), PVDF-HFP (0.96 mS cm^{-1}), HFP-EMIM (1.04 mS cm^{-1}), and HFP/PEO (1.46 mS cm^{-1}). This enhancement is attributed to the formation of an interconnected 3D porous structure, which facilitates continuous Li^+ transport. The addition of PEO reduces crystallinity, thereby promoting amorphous regions that support ion mobility, while the presence of EMIMTFSI further enhances ionic movement by reducing ion-pairing interactions and providing additional conduction channels. To investigate the interfacial compatibility between the GPEs and electrodes, electrochemical impedance spectroscopy (EIS) was conducted. As shown in **Fig. 3b** and **Fig. S16**, HFP/PEO-EMIM exhibited the lowest interfacial resistance (80.8 Ω) compared to PP (118 Ω), PVDF-HFP (107 Ω), HFP/PEO (92.4 Ω), and HFP-EMIM (88.5 Ω). This reduction in interfacial resistance indicates that the introduction of EMIMTFSI can effectively enhance the interface compatibility between the electrolyte and the electrodes, and improve charge transfer dynamics, in agreement with previous contact angle and electrolyte uptake results. The electrochemical stability of the GPEs was assessed by linear sweep voltammetry (LSV). As depicted in **Fig. 3c** and **Fig. S17**, HFP/PEO-EMIM demonstrated an extended electrochemical window of 4.69 V (vs. Li/Li^+), compared to 4.58 V, 4.62 V, 4.64 V, and 4.66 V for PP, PVDF-HFP, HFP/PEO, and HFP-EMIM, respectively. This improvement confirms the stabilizing effect of EMIMTFSI, which suppresses electrolyte decomposition and enables compatibility with high-voltage cathode materials. To further elucidate the Li^+ transport characteristics, the Li^+ transference number (t_{Li+}) was evaluated (**Fig. 3d**, **Fig. S18**). HFP/PEO-EMIM achieved a notably high t_{Li+} of 0.68, outperforming PP (0.45), PVDF-HFP (0.50), HFP-EMIM (0.52), and HFP/PEO (0.65), which was consistent with the competitive coordination mechanism revealed by DFT and FTIR.

To evaluate the Li^+ reaction kinetics in different gel polymer electrolyte systems, cyclic voltammetry (CV) was performed on LFP||Li full cells. As shown in **Fig. 3e**, the HFP/PEO-EMIM-based cell exhibited the highest current response and the smallest redox peak separation (ΔE_p = 0.381 V), indicating reduced polarization and faster Li^+ transfer kinetics compared to PVDF-HFP and HFP/PEO. Additionally, the nearly overlapping CV curves of HFP/PEO-EMIM in repeated scans (**Fig. S19**) demonstrate excellent electrochemical reversibility and interfacial stability. The symmetric redox peaks observed across varied scan rates (**Fig. S20**) further confirm the enhanced electrochemical kinetics of the HFP/PEO-EMIM system. To further probe the Li plating/stripping behavior, CV and Coulombic efficiency (CE) tests were conducted in Li||Cu cells. As depicted in **Fig. 3f** and **Fig. S21**, the HFP/PEO-EMIM electrolyte delivered the highest average CE of ~98% over 120 cycles, outperforming

PP (~96%, unstable after 50 cycles), PVDF-HFP (~92%, unstable over 100 cycles), and HFP/PEO (~96%, declining after 110 cycles). This superior reversibility indicates that HFP/PEO-EMIM effectively facilitates uniform Li deposition and dissolution on Cu substrates.

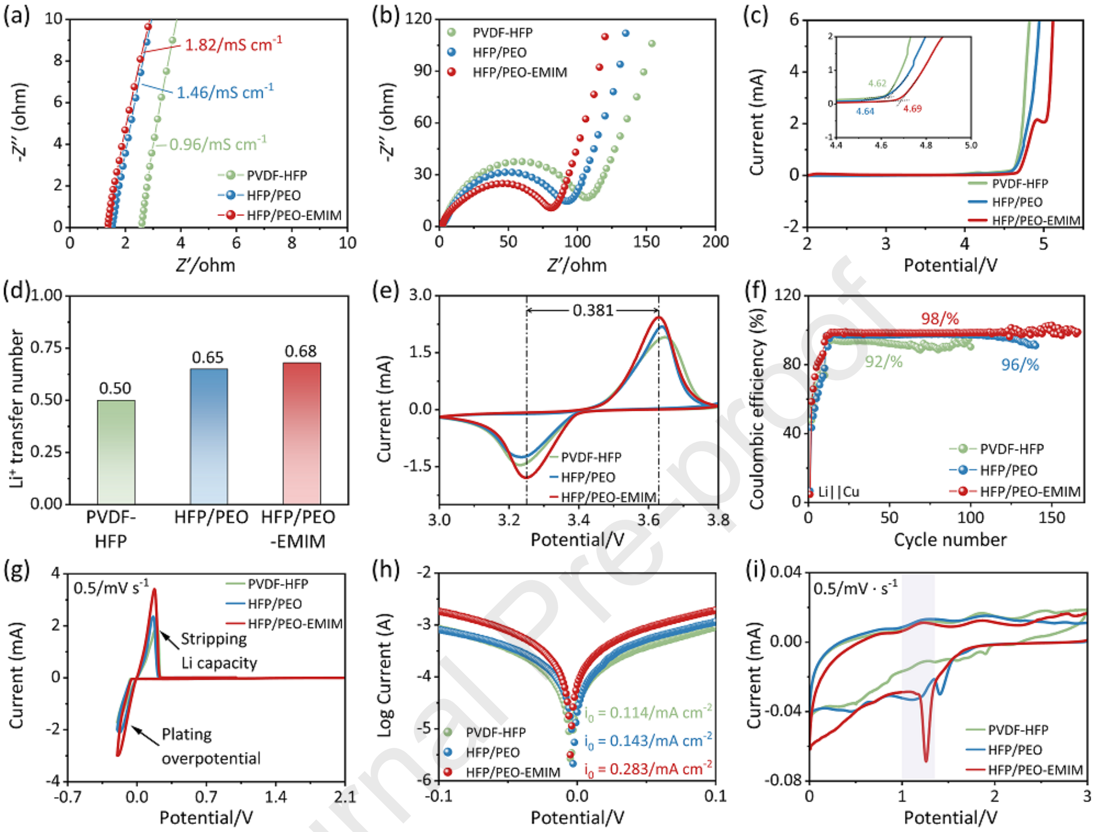

Fig. 3. (a) Ionic conductivity of the electrolytes. (b) EIS of LFP||Li cells. (c) LSV curves. (d) Li$^+$ transference numbers. (e) CV curves of LFP||Li cells with PVDF-HFP, HFP/PEO, and HFP/PEO-EMIM. (f) Coulombic efficiencies of Li||Cu cells employing PVDF-HFP, HFP/PEO, and HFP/PEO-EMIM. (g) CV curves of Li||Cu cells within the voltage range of −0.2 to 1 V. (h) Tafel plot. (i) CV curves of Li||Cu cells from 0 to 3 V.

Moreover, the HFP/PEO-EMIM system exhibited significantly higher plating/stripping current densities (**Fig. 3g**, **Fig. S22**), reflecting accelerated charge transfer kinetics. The larger enclosed area in its CV curves and its lowest nucleation overpotential further confirm improved redox kinetics and favorable lithium deposition behavior. These enhancements stem from the synergistic effects of PEO-derived ether-oxygen coordination with Li$^+$ and the plasticizing, ion-mobilizing function of EMIMTFSI, which together lower energy barriers for Li$^+$ transport. To quantitatively evaluate interfacial kinetics at the Li metal anode, exchange current densities (i_0) were derived from Tafel plots. HFP/PEO-EMIM demonstrated the highest i_0 value (0.283 mA cm^{-2}), significantly exceeding those of PP (0.087 mA cm^{-2}), PVDF-HFP (0.114 mA cm^{-2}), and HFP/PEO (0.143 mA cm^{-2}) (**Fig. 3h** and **Fig.**

S23). This suggests superior interfacial charge transfer kinetics, attributable to improved electrolyte wettability, optimized ion diffusivity, and formation of a stable low-resistance electrolyte/Li interface. Collectively, these results affirm that the HFP/PEO-EMIM gel electrolyte not only accelerates Li^+ transport and enhances reaction kinetics but also suppresses dendritic growth and parasitic side reactions, ultimately contributing to improved electrochemical reversibility and prolonged cycling performance in lithium metal batteries. To further understand the effect of the proposed electrolyte on interfacial stability, the SEI formed on the Li-metal surface was investigated. CV measurements were conducted to examine the redox reactions associated with SEI formation. As shown in **Fig. 3i** and **Fig. S24**, a distinct reduction peak at 1.25 V appeared in the initial scan of the HFP/PEO-EMIM system, which is attributed to the dissociation of $TFSI^−$ anions. This suggests that the presence of EMIMTFSI promotes preferential $TFSI^−$ decomposition at the anode interface, thereby facilitating the formation of an inorganic-rich SEI and inhibiting SEI rupture and regeneration.

2.4 Li plating/stripping behavior and stability

To evaluate the Li anode protection capability of different GPEs, symmetric Li||Li cells were assembled for cycling and rate performance assessments. As illustrated in **Fig. 4a** and **Fig. S25**, the cell using PP showed a significant and unstable increase in overpotential after 200 h of cycling. In comparison, the PVDF-HFP and HFP/PEO systems exhibited initially increasing and subsequently decreasing polarization trends, likely due to the accumulation of inactive “dead Li” and increased interfacial impedance caused by continuous electrolyte decomposition. In contrast, the HFP/PEO-EMIM-based cell maintained a low and stable overpotential of 11 mV over 3200 h at 1 mA cm^{-2} and 1 mAh cm^{-2}. Even after 3400 h, the overpotential remained as low as 9.1 mV, suggesting suppressed side reactions and sustained reaction kinetics. This stable behavior implies minimal active lithium loss and negligible “dead Li” accumulation over extended cycling. The rate performance of the HFP/PEO-EMIM system further confirms its robustness under elevated current densities (**Fig. 4b** and **Fig. S26**). Stepwise increases in current density from 0.5 to 5 mA cm^{-2} resulted in corresponding, yet controlled, increases in overpotential without short-circuiting, highlighting excellent electrochemical stability and rate capability. These improvements are ascribed to the synergistic effect between the ether-oxygen groups in PEO and the $EMIM^+$ cations, which together enhance lithium-ion transport and enable uniform Li deposition. Additionally, the incorporation of EMIMTFSI increases the participation of $TFSI^-$ anions in the Li^+ solvation sheath, thereby promoting their preferential reduction and facilitating the formation of an SEI enriched in LiF and Li_3N. To further validate the superior compatibility of HFP/PEO-EMIM under high-stress conditions, symmetric Li||Li cells were subjected to testing at higher current densities. As shown in **Fig. 4c-d** and **Fig. S27-S28**, the HFP/PEO-EMIM system consistently exhibited lower polarization voltages and improved cycling durability compared to PP, PVDF-HFP, and HFP/PEO, even at 2 and 5 mA cm^{-2}. These results confirm that HFP/PEO-EMIM effectively regulates lithium-ion transport, promotes uniform deposition, and enables highly reversible Li plating/stripping.

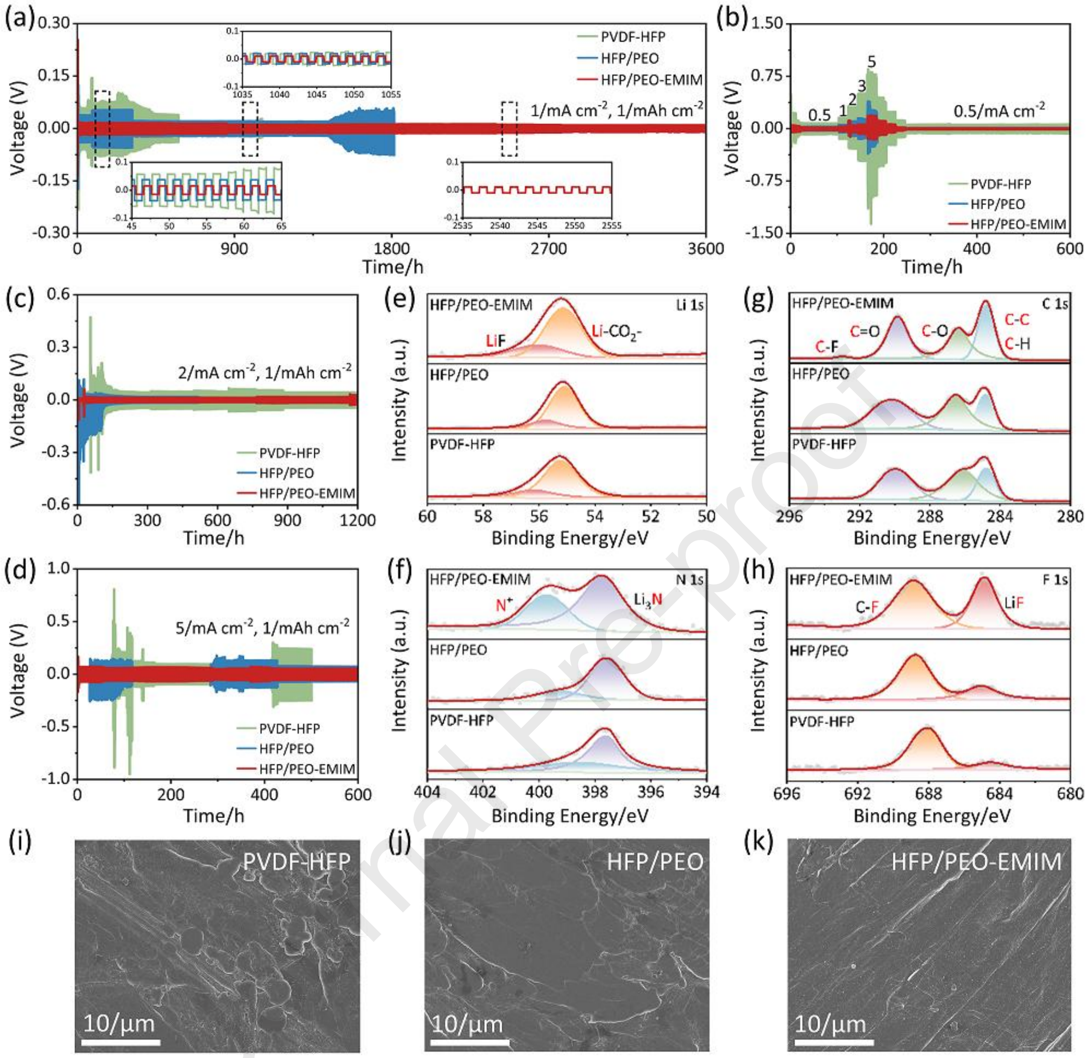

Fig. 4. (a) Cycling performance of Li||Li symmetric cells with PVDF-HFP, HFP/PEO, and HFP/PEO-EMIM at 1 mA cm^{-2} and 1 mAh cm^{-2}. (b) Rate capabilities of the Li||Li symmetric cells. (c-d) Cycling performances at 2 and 5 mA cm^{-2}, respectively. (e-h) XPS spectra of Li anodes after cycling with PVDF-HFP, HFP/PEO, and HFP/PEO-EMIM. (i-k) SEM images of Li anodes after cycling.

To evaluate the effect of GPEs on the Li metal anode and determine the chemical composition of the cycled SEI layer, symmetric Li||Li cells were disassembled after cycling, and the Li surface chemical state were characterized via XPS. The analysis revealed that the SEI layers were primarily composed of carbonaceous organic species (C–O, C=O) and inorganic components (LiF, Li_3N), originating from the decomposition of electrolyte solvents and TFSI$^-$ anions. The inorganic species, characterized by high ionic conductivity and insolubility, enable rapid Li$^+$ transport across the SEI layer, reduce local Li$^+$ depletion at the interface, and promote uniform ion migration. These effects collectively suppress lithium dendrite growth and enhance SEI stability-both of which are critical for achieving long-term cycling performance of lithium metal anodes. As shown in **Fig. 4e**, peaks located at 56.2 eV and 55.2 eV correspond to LiF and Li_2CO_3-related species, respectively. In the C 1s spectrum (**Fig. 4g**), peaks at 292.51 eV, 289.95 eV, 286.25 eV, and 284.80 eV are assigned to C–F, C=O, C–O, and C–C/C–H bonds, mainly derived from organic compounds generated during electrolyte decomposition. Notably, the N 1s spectrum in **Fig. 4f** displayed a peak at 397.59 eV corresponding to Li_3N. The relative intensity of this peak was significantly higher for the HFP/PEO-EMIM system than for PP, PVDF-HFP, and HFP/PEO, suggesting a presence of Li_3N in the SEI layer (**Fig. S29**). A similar trend is observed in the F 1s spectrum (**Fig. 4h**), where the LiF peak at 685.13 eV is most prominent in the HFP/PEO-EMIM system. These results indicate that, in the HFP/PEO-EMIM electrolyte, the decomposition of the solvent is effectively suppressed, while $TFSI^-$ anions preferentially decompose to yield stable inorganic species, promoting the formation of a robust, inorganic-rich SEI layer. This behavior is attributed to the ability of $EMIM^+$ and $TFSI^-$ to modulate the Li^+ solvation environment, thereby facilitating the aggregation and subsequent decomposition of solvation structures at the lithium interface. Complementary surface morphology analysis via SEM (**Fig. 4i-k**, **Fig. S30**) further supports these findings. After cycling, the SEI layer in the PP system exhibits inhomogeneous morphology, characterized by irregular clusters and non-uniform height distribution. PVDF-HFP and HFP/PEO also exhibit uneven, block-like surface features. In contrast, the lithium surface cycled in HFP/PEO-EMIM presents a smooth, compact, and particle-free morphology, indicating the formation of a dense and uniform SEI. This morphological uniformity results from the synergistic effects of enhanced ionic conductivity and anion-derived SEI formation, which collectively facilitate homogeneous Li deposition, suppress parasitic reactions, and effectively inhibit dendritic growth.

2.5 Interfacial chemistry and SEI composition

The electrochemical stability of battery components is primarily determined by the energies of their highest occupied molecular orbitals (HOMO) and lowest unoccupied molecular orbitals (LUMO). Density functional theory (DFT) calculations (**Fig. 5a**) reveal that EMIMTFSI (−2.447 eV), LiTFSI (−1.794 eV), and $LiNO_3$ (−2.303 eV) possess significantly lower LUMO energy levels than DOL (1.387 eV), DME (1.343 eV), and HFP/PEO (−0.981 eV). These lower LUMO values indicate stronger electron affinity and a higher propensity for reduction at the anode interface, facilitating their decomposition into inorganic species such as LiF and Li_3N, which contribute to the formation of inorganic-rich SEI layers. Furthermore, EMIMTFSI and LiTFSI exhibit lower HOMO energy levels compared to DOL, DME, and LiNO3, suggesting superior oxidative stability due to the electron-withdrawing characteristics of their fluorine-containing moieties. Electrostatic potential (ESP) mapping (**Fig. 5b**) further supports this, showing stronger Li^+-$TFSI^−$ interactions compared to $EMIM^+$-$TFSI^−$, as evidenced by lower ESP values. This enhanced electrostatic attraction promotes the incorporation of $TFSI^−$ anions into Li^+ solvation sheaths, which subsequently undergo reduction at the lithium surface, yielding an inorganic SEI.

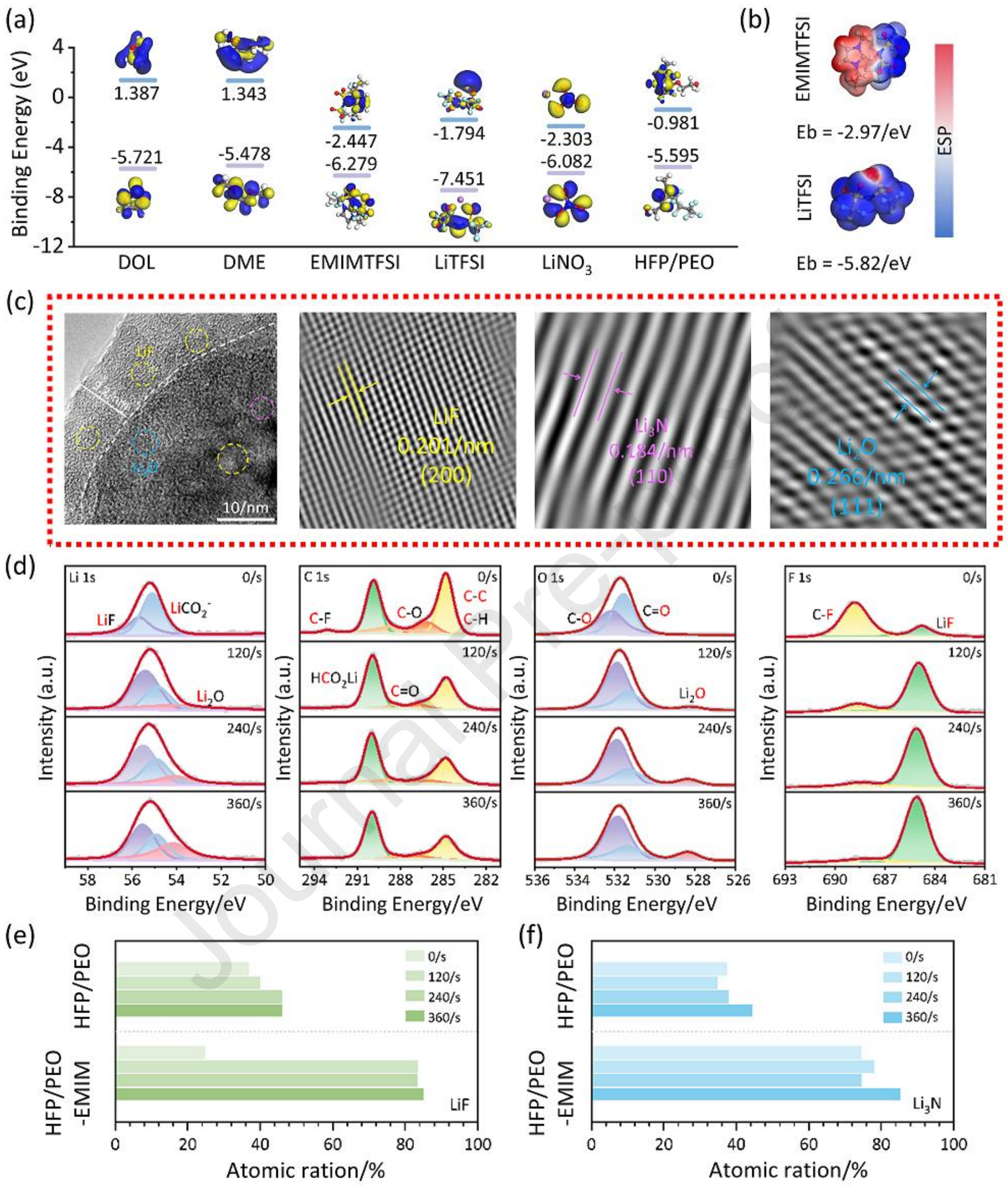

Fig. 5. (a) Calculated energy levels of the HOMO and LUMO orbitals. (b) Electrostatic potential distributions of LiTFSI and EMIMTFSI molecules. (c) TEM images of the cycled Li anodes. (d) XPS depth profiles of cycled Li anodes from the LFP||HFP/PEO-EMIM||Li cell. (e,f) LiF and Li_3N content at different etching depths of cycled Li anodes from HFP/PEO and HFP/PEO-EMIM.

To validate the computational predictions, the SEI layer formed in the HFP/PEO-EMIM gel electrolyte system was characterized by high-resolution transmission electron microscopy (HR-TEM) after 500 cycles in an LFP||Li full cell.

This technique enabled direct visualization of both the chemical composition and nanostructure of the SEI. As shown in **Fig. 5c**, the SEI exhibited a thickness of approximately 9.2 nm. It displayed a multiphase nanostructure comprising abundant inorganic nanocrystalline domains embedded within an amorphous matrix. Identification of these inorganic species was accomplished by correlating the observed lattice spacings with reference crystal planes. Clear lattice fringes corresponding to the LiF (002) plane (0.201 nm), Li_3N (110) plane (0.184 nm), and Li_2O (111) plane (0.266 nm) were observed. These findings confirm that the HFP/PEO-EMIM electrolyte promotes the formation of an anion-derived, inorganic-rich SEI layer. Such a layer exhibits a high lithium-ion diffusion coefficient and enhanced mechanical strength, which together facilitate uniform lithium deposition and effectively suppress dendrite growth. Further corroboration of the computational and TEM results was obtained via XPS. As shown in **Fig. 5d**, depth-profiling XPS analysis was performed with sputtering for 0, 120, 240, and 360 seconds to reveal the compositional evolution from the outer to the inner region of the SEI. At the outermost surface (0 s etch), the Li 1s spectrum displayed a peak at 55.1 eV corresponding to $LiCO_2^-$. In the C 1s spectrum, peaks at 289.79 eV ($LiCO_2H$), 288.69 eV (C=O), 286.09 eV (C–O), and 284.8 eV (C–C) were observed, while the O 1s spectrum featured peaks at 532.19 eV (C–O) and 531.59 eV (C=O). These peaks collectively represented decomposition products of the electrolyte solvent. Notably, with increasing etching time, the intensities of these peaks decreased progressively, indicating that these organic components were primarily located near the outer surface of the SEI. Importantly, the Li 1s spectrum also displayed a peak at 54 eV, attributed to Li_2O, which was corroborated by a corresponding peak at 528.5 eV in the O 1s spectrum. In the F 1s spectrum, a C–F peak at 688 eV matched the C–F signal at 293.08 eV in the C 1s spectrum, whereas the LiF peak at 684.5 eV corresponded to the LiF signal at 55.49 eV in the Li 1s spectrum. As sputtering progressed, the intensity of the Li-F signal markedly exceeded that of the C–F signal, supporting preferential formation of inorganic LiF deeper within the SEI. Additionally, the N 1s spectrum revealed a peak at 396.99 eV, assigned to Li_3N. In the S 2p region, peaks at 161.0 eV and 159.5 eV were attributed to Li_2S_2 and Li_2S, respectively. The intensities of Li_3N and sulfur-containing species increased with etching depth, as shown in **Fig. S31**. The LiF content of HFP/PEO-EMIM under etching for 0, 120, 240, and 360 seconds is 24.57%, 83.39%, and 83.31%, 85.05%, respectively. These values are higher compared to the SEI formed using HFP/PEO, which has LiF content of 36.72%, 39.89%, 45.91%, and 46.18% for the same etching times (**Fig. 5e**). Meanwhile, The Li_3N content of HFP/PEO-EMIM is also higher than HFP/PEO (**Fig. 5f**). To further evaluate the lateral uniformity of the SEI, EDS elemental mapping and line-scan analysis were performed. The EDS maps revealed a homogeneous distribution of F, S, and N across the Li surface, indicating that inorganic species uniformly cover the electrode (**Fig. S32**). Line-scan profiles further confirm that the F, S, and N signal intensities remained stable over 30 μm with negligible fluctuations (**Fig. S33**), which was consistent with the depth-profiling XPS results. These results collectively demonstrate that during initial cycling, the HFP/PEO-EMIM system suppresses solvent decomposition and promotes preferential TFSI$^-$ anion reduction on the lithium surface, forming a dense, inorganic-rich SEI composed of LiF, Li_2O, Li_3N, Li_2S_2, and Li_2S. This robust SEI not only suppresses dendrite initiation and growth but also reduces interfacial reactivity, thereby significantly extending battery cycle life.

2.6 Full-cell performance

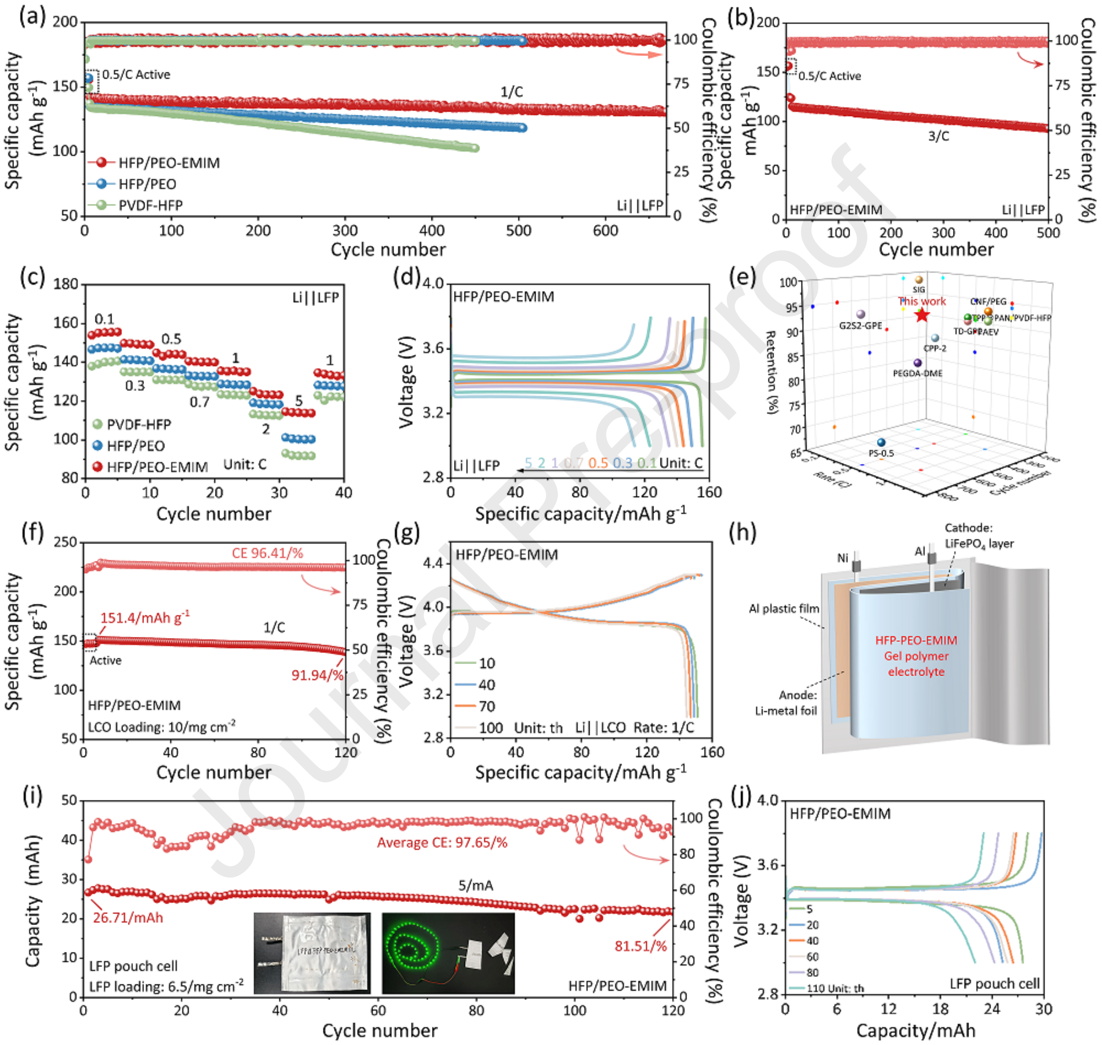

Fig. 6. (a) Cycling performances of LFP||Li full cells incorporating PVDF-HFP, HFP/PEO, and HFP/PEO-EMIM at 1 C. (b) Cycling performance of the LFP||HFP/PEO-EMIM||Li cell at 3 C. (c) Rate capabilities of the LFP||Li full cells. (d) Charge/discharge profiles of the LFP||HFP/PEO-EMIM||Li cell at various rates. (e) Comparative performance analysis with reported data in the literature. (f) Cycling performance of the LCO||HFP/PEO-EMIM||Li cell at 1 C. (g) Charge/discharge profiles of the LCO||HFP/PEO-EMIM||Li cell at selected cycles. (h) Illustration of the structure of the LFP||HFP/PEO-EMIM||Li pouch cell. (i) Long-term cycling performance of the pouch cell. (j) Charge/discharge profiles of the pouch cell at selected cycles.

To evaluate the practical applicability of the GPEs, $LiFePO_4$ (LFP)||Li full cells were assembled. As shown in **Fig. 6a** and **Fig. S34**, the HFP/PEO-EMIM-based electrolyte delivered an initial specific capacity of 142.4 mAh g^{-1} at 1 C, slightly surpassing that of PP (141.5 mAh g^{-1}), PVDF-HFP (137.4 mAh g^{-1}), and HFP/PEO (134.9 mAh g^{-1}). Remarkably, the HFP/PEO-EMIM cell retained a capacity of 130.9 mAh g^{-1} after 650 cycles, corresponding to a high capacity retention of 95% and near-unity Coulombic efficiency. This outstanding cyclability was attributed to the formation of a robust and stable electrode/electrolyte interphase, in contrast to capacity retentions of 87.9%, 77.7%, and 89.6% after 180, 450, and 500 cycles for PP, PVDF-HFP, and HFP/PEO electrolytes, respectively. Detailed capacity retention at intermediate cycles further confirms the superior long-term stability of HFP/PEO-EMIM, maintaining 136.5, 135.1, 133.2, and 131.8 mAh g^{-1} after the 100, 200, 300, and 400cycles (**Fig. S35**). Moreover, minimal voltage polarization was observed across cycles, indicating excellent electrochemical reversibility. Post-cycling EIS measurements revealed the lowest interfacial resistance for HFP/PEO-EMIM (92.3 Ω), outperforming PP (133 Ω), PVDF-HFP (126 Ω), and HFP/PEO (103 Ω), as shown in **Fig. S36**, reflecting a highly stabilized interface via uniform SEI formation. SEM analysis of cycled lithium anodes (**Fig. S37**) revealed significant dendritic and uneven deposition in PP and PVDF-HFP cells, while HFP/PEO exhibited irregular clusters. In contrast, HFP/PEO-EMIM enabled the formation of dense, flat lithium deposits, confirming effective dendrite suppression. XRD characterization (**Fig. S38**) revealed peak sharpening and crystallinity increase in PVDF-HFP and HFP/PEO after cycling, indicating structural damage. Meanwhile, the HFP/PEO-EMIM structure remained relatively intact. XPS analysis (**Fig. S39**) demonstrated that the elemental composition of the electrolytes remained stable before and after cycling, further supporting the chemical stability of the GPEs. As shown in **Fig. S40**, the tensile tests after the cycle indicated that the tensile strength and elongation at break of PP, PVDF-HFP, and HFP/PEO decreased significantly after the cycle. The tensile strength of HFP/PEO-EMIM also decreased, but it still had the largest tensile strength compared to the others, and the elongation at break only showed a small change compared to the original state. This indicated that the structure of HFP/PEO-EMIM changed minimally during the cycle, which ensured the continuous resistance to mechanical deformation and lithium dendrite penetration.

Encouragingly, the HFP/PEO-EMIM electrolyte maintained excellent electrochemical performance even under high current densities. At 3 C (**Fig. 6b**), it retained 75% of its initial capacity (125.1 mAh g^{-1}) after 500 cycles, highlighting its strong rate capability due to the integrity of the SEI under severe polarization. Rate performance tests (**Fig. 6c**, **Fig. S41**) further verified this, showing capacities of 155, 149, 144, 140, 135, 123, and 114 mAh g^{-1} at 0.1-5 C. Upon returning to 1 C, a specific capacity of 133 mAh g^{-1} was recovered, indicating excellent reversibility. A comparative plot (**Fig. 6d**, **Fig. S42**) clearly illustrated the superior rate performance of HFP/PEO-EMIM over other systems. Notably, its galvanostatic charge-discharge curves exhibited well-defined voltage plateaus across all current densities, indicating stable intercalation/deintercalation behavior at the LFP cathode. Finally, benchmarking against state-of-the-art GPEs reported in the literature [38-46] (**Fig. 6e**,

Table S1), HFP/PEO-EMIM GPE demonstrated clear advantages in terms of initial specific capacity, long cycle life, and capacity retention, confirming its potential as a high-performance electrolyte for advanced lithium metal batteries.

To assess broader applicability, the compatibility of HFP/PEO-EMIM with high-voltage cathodes was evaluated using $LiCoO_2$ (LCO)||Li full cells. As shown in **Fig. 6f**, the cell delivered an initial specific capacity of 151.4 mAh g^{-1} with 91.94% capacity retention after 120 cycles and an average (CE of 96.41%, demonstrating stable operation under high-voltage conditions. Additionally, the nearly overlapping charge-discharge voltage profiles (**Fig. 6g**) exhibited minimal polarization evolution, confirming excellent cycling reversibility. The practical feasibility of the HFP/PEO-EMIM electrolyte was further demonstrated in a pouch cell configuration. As shown in **Fig. 6h**, the HFP/PEO-EMIM gel electrolyte was successfully integrated into a 7 cm×8 cm LFP-based pouch cell (active material loading: 6.5 mg cm^{-2}). This cell delivered an initial discharge capacity of 26.71 mAh and retained 81.51% capacity after 120 cycles, maintaining an average CE above 97% (**Fig. 6i**). Its galvanostatic charge-discharge curves closely resembled those of button cells, with negligible polarization throughout cycling. Notably, this smooth voltage profile persisted after 110 cycles, indicating stable and efficient electrochemical conversion. To further examine safety performance, mechanical deformation tests were conducted. As shown in **Fig. S43**, the assembled pouch cell continued powering an LED light strip when folded to 90°, 135°, and 180°, with full functionality restored upon unfolding. Even after repeated cutting (**Fig. S44**), the cell remained operational and showed no signs of short-circuiting or combustion, underscoring the excellent mechanical and thermal safety of the HFP/PEO-EMIM gel electrolyte.

These findings collectively highlight the HFP/PEO-EMIM electrolyte's strong potential for integration into practical Li battery systems. To provide a comprehensive comparison, a radar chart (**Fig. S45**) was constructed to evaluate five key performance metrics. Compared with PP, PVDF-HFP, and HFP/PEO systems, HFP/PEO-EMIM demonstrated significant advantages in high-voltage stability, ionic conductivity, electrode compatibility, rate capability, and cycling stability. These enhancements stem from the synergistic interactions between the polymer matrix and ionic liquid, which collectively promote faster Li^+ transport, enhance interfacial stability, facilitate the formation of robust SEI layers, and effectively suppress lithium dendrite formation.

3. Conclusions

In summary, a novel ionic liquid-modified composite gel polymer electrolyte (HFP/PEO-EMIM) was successfully constructed by integrating EMIMTFSI into a rationally engineered "rigid-flexible" polymer matrix. This architecture synergistically combines the thermal/mechanical robustness of PVDF-HFP, the Li^+-coordinating ability of PEO, and the interfacial-modifying properties of EMIMTFSI to fulfil the requirements for high-performance gel electrolytes. The confined incorporation of ionic liquid within the polymer network not only suppresses phase separation and enhances bulk ionic transport, but also contributes to the formation of an inorganic-rich, stable SEI layer at the Li interface. Electrochemical evaluations confirm that the HFP/PEO-EMIM delivers remarkable performance in both symmetric and full-cell configurations. Specifically, the symmetric Li|| HFP/PEO-EMIM||Li cell exhibits highly stable and dendrite-free cycling exceeding 3500 h, highlighting its long-term interfacial stability. In practical full-cell tests, LFP||HFP/PEO-EMIM||Li devices retain high capacity over extended cycling, even under high current conditions (*e.g.*, 3 C), demonstrating excellent rate capability and structural durability. Beyond performance metrics, this work provides new mechanistic insights into electrolyte-electrode interactions enabled by ionic liquid engineering. It further validates a design paradigm that leverages polymer-IL synergy to tailor SEI chemistry and lithium deposition behavior. These findings offer a promising pathway toward the development of intrinsically safe, high-energy-density Li-ion batteries with robust interfacial properties and long-term cycling reliability.

4. Experimental section

4.1. Preparation of fiber membrane

To prepare the precursor solution, 2 g of PVDF-HFP was dissolved in 10 mL of DMF and stirred magnetically at 70 °C for 6 h. PEO (10 wt%, vacuum-dried at 60 °C for 6 h prior to use) was subsequently added and stirred for another 12 h at the same temperature to form the electrospinning solution. The HFP/PEO fibrous membrane was fabricated via electrospinning with a solution flow rate of 1.5 mL h^{-1}, a tip-to-collector distance of 13-15 cm, and an applied voltage of 15 kV. The electrospinning was performed under controlled humidity (40±5%) and temperature (30±5 °C). The collected membrane was dried at 60 °C for 12 h to remove residual solvents. The final obtained fibrous membrane was named HFP/PEO.

4.2. Preparation of HFP/PEO-EMIM GPE

The electrolyte used for membrane soaking was 1.0 M lithium bis(trifluoromethanesulfonyl)imide (LiTFSI) dissolved in a mixed solvent of 1,3-dioxolane (DOL) and 1,2-dimethoxyethane (DME) (1:1 v/v) with 1% LiNO3 additive. The dried HFP/PEO membrane was soaked in a mixture of EMIMTFSI and the above conventional electrolyte at a volume ratio of 1:3 until saturation. The excessive solution on the surface was removed using lint-free paper, and the final gel electrolyte contains both the ionic liquid and the conventional electrolyte components. HFP/PEO-EMIM gel electrolyte was obtained. Only by immersing in the electrolyte solution could PVDF-HFP and HFP/PEO gel electrolytes be obtained. All of the above operations were carried out in the glove box.

4.3.Preparation of Cathodes

The cathode slurry was prepared by dispersing $LiFePO_4$, Super P, and PVDF in NMP at a mass ratio of 8:1:1. The mixture was stirred for 6 h to obtain a homogeneous slurry, which was then coated onto aluminum foil and dried under vacuum at 80 °C for 12 h. The loading was controlled at 5±0.5 mg cm^{-2}, and the electrodes were punched into 12 mm diameter discs.

References

[1] T. Deng, C. Wang, H. Wan, A.M. Li, X. He, Z. Wang, L. Cao, X. Fan, C. Wang, A universal design of lithium anode via dynamic stability strategy for practical all-solid-state batteries, Angewandte Chemie International Edition 64 (2025) e202418811.
[2] P. Chang, Z. Liu, M. Xi, Y. Guo, T. Wu, J. Ding, H. Liu, Y. Huang, Frustrated lewis pairs regulated solid polymer electrolyte enables ultralong cycles of lithium metal batteries, Advanced Powder Materials 4 (2025) 100263.
[3] C. Chen, X. Yang, W. Zhou, L. Yu, Dendrite-free Li metal anode achieved by bi-functional host of NH_2-modified UiO-66 on Zn-embedded porous carbon nanofibers, Advanced Functional Materials 35 (2025) 2501846.
[4] Q. Guo, Y. Cai, L. Chen, Z. Lin, B. Gao, X. Zhang, X. Zhu, Y. Zheng, Z. Li, K. Huo, Competitive solvation chemistry modulated nonflammable pseudo ultralow concentration electrolyte toward high-voltage Li metal batteries, Advanced Functional Materials 35 (2025) 2500500.
[5] S. Li, H. Hong, X. Yang, D. Li, Q. Xiong, D. Zhang, S. Wang, Z. Huang, H. Lv, C. Zhi, In situ polymerized polyfluorinated crosslinked polyether electrolytes for high-voltage lithium metal batteries, Advanced Materials 37 (2025) 2504333.
[6] X. Zhang, X. Liu, A. Jia, B. Song, W. Gao, L. He, B. Zhou, K. Hu, H. Zhang, Y. Wu, J. He, Z. Zhang, Sb-terminated functionalized interlayer with dual-function mechanism enables highly stable lithium metal batteries, Advanced Powder Materials 5 (2026) 100365.
[7] H. Chen, X. Li, M. Ling, X. Gao, D. Zhao, Z. Chen, Dense nano-tips homogenize lithium deposition, Advanced Powder Materials 5 (2026) 100401.
[8] Z. Zhao, X. Zhao, Y. Zhou, S. Liu, G. Fang, S. Liang, Towards establishing uniform metrics for evaluating the safety of lithium metal batteries, Advanced Powder Materials 2 (2023) 100139.
[9] B. Sun, L. Kuang, M. He, Q. Zhang, Y. Guan, C. Zhang, D. Zhang, C. Pei, P. Li, S. Ni, Insertion type Li_3VO_4 lithiophilic sites boosting dendrite-free lithium deposition in trapping-and-leveling model, Advanced Energy Materials 15 (2025) 2405307.
[10] S. Li, X. Kong, X.S. Zhang, W. Liu, H. Luo, Q. Yang, Z. Li, Y. Zhang, B. Li, W.P. Wang, S. Xin, D. Zhang, A bismuth-derived, inorganic-rich artificial solid electrolyte interphase enables a stable and dendrite-free lithium-metal anode in rechargeable batteries, Advanced Energy Materials 16 (2025) e04379.
[11] R. Zhao, Y. Gao, Z. Qin, Y. Li, T. Zhang, A. Pan, N. Zhang, R. Ma, X. Liu, G. Chen, Regulating electric double layer in non-fluorinated ether electrolyte enables high-voltage and low-temperature lithium metal batteries, Advanced Powder Materials 4 (2025) 100296.

[12] H. Huang, C. Liu, Z. Liu, Y. Wu, Y. Liu, J. Fan, G. Zhang, P. Xiong, J. Zhu, Functional inorganic additives in composite solid-state electrolytes for flexible lithium metal batteries, Advanced Powder Materials 3 (2024) 100141.

[13] M. Zhu, J. Wu, Y. Wang, M. Song, L. Long, S. H. Siyal, X. Yang, G. Sui, Recent advances in gel polymer electrolyte for high-performance lithium batteries, Journal of Energy Chemistry 37 (2019) 126-142.

[14] X. Zeng, L. Dong, J. Fu, L. Chen, J. Zhou, P. Zong, G. Liu, L. Shi, Enhanced interfacial stability with a novel boron-centered crosslinked hybrid polymer gel electrolytes for lithium metal batteries, Chemical Engineering Journal 428 (2022) 131100.

[15] S.H. Kim, N. Park, W. Bo Lee, J.H. Park, Functional sulfate additive-derived interfacial layer for enhanced electrochemical stability of PEO-based polymer electrolytes, Small 20 (2024) 2309160.

[16] L. Ma, J. Tan, Z. Ren, B. Feng, Z. Liu, P. Yi, S. Cao, W. Lu, Y. Liu, C. Ye, M. Ye, H. Fang, J. Shen, Designing bilayer heterostructure functional polymer electrolytes with interfacial engineering strategy for high-performance lithium metal batteries, Advanced Functional Materials 35 (2025) 2414816.

[17] Y. Ma, Y. Qiu, K. Yang, S. Lv, Y. Li, X. An, G. Xiao, Z. Han, Y. Ma, L. Chen, D. Zhang, W. Lv, Y. Tian, T. Hou, M. Liu, Z. Zhou, F. Kang, Y.B. He, Competitive Li-ion coordination for constructing a three-dimensional transport network to achieve ultra-high ionic conductivity of a composite solid-state electrolyte, Energy & Environmental Science 17 (2024) 8274-8283.

[18] Q. Zhou, J. Ma, S. Dong, X. Li, G. Cui, Intermolecular chemistry in solid polymer electrolytes for high-energy-density lithium batteries, Advanced Materials 31 (2019) 1902029.

[19] L. Han, L. Wang, Z. Chen, Y. Kan, Y. Hu, H. Zhang, X. He, Incombustible polymer electrolyte boosting safety of solid-state lithium batteries: a review, Advanced Functional Materials 33 (2023) 2300892.

[20] P. Li, Y. Huang, Y. Yu, X. Ma, Z. Wang, G. Shao, Recent advances and future prospects for PVDF-based solid polymer electrolytes, Journal of Power Sources 628 (2025) 235855.

[21] Q. Wang, F. Liu, Z. Qi, G. Qin, L. Wang, X. He, Uv-triggered in situ formation of a robust SEI on black phosphorus for advanced energy storage: Boosting efficiency and safety via rapid charge integration plasticity, Advanced Energy Materials 15 (2025) 2403188.

[22] T. Yang, X. Xu, S. Chen, Y. Yang, F. Li, W. Fan, Y. Wu, J. Zhao, J. Liu, Y. Huo, A lithiophilic donor-acceptor polymer modified separator for high-performance lithium metal batteries, Angewandte Chemie International Edition 64 (2025) e202420973.

[23] Y. Zhai, W. Hou, M. Tao, Z. Wang, Z. Chen, Z. Zeng, X. Liang, P. Paoprasert, Y. Yang, N. Hu, S. Song, Enabling high-voltage “superconcentrated ionogel-in-ceramic” hybrid electrolyte with ultrahigh ionic conductivity and single Li^+-ion transference number, Advanced Materials 34 (2022) 2205560.

[24] L. Cui, S. Zhang, J. Ju, S. Liu, H. Wang, J. Xu, W. Zhang, P. Mu, Y. Zhang, L. Liu, P. Xu, P. Han, Z. Lv, G. Cui, Quantification and optimization of interfacial ion transport in polymer/ceramic composite electrolytes for solid-state batteries, Angewandte Chemie International Edition 64 (2025) e202517153.

[25] D. Zhou, D. Shanmukaraj, A. Tkacheva, M. Armand, G. Wang, Polymer electrolytes for lithium-based batteries: Advances and prospects, Chem 5 (2019) 2326-2352.

[26] H. Huang, S. Liu, Y. Xie, J. Liu, C. Shi, M. Sun, H. Peng, J. Lan, Y.P. Deng, L. Huang, S.G. Sun, Constructing an artificial interface as a bifunctional promoter for the Li anode and the NCM cathode in lithium metal batteries, Journal of the American Chemical Society 146 (2024) 31137-31149.

[27] X. Tang, S. Lv, K. Jiang, G. Zhou, X. Liu, Recent development of ionic liquid-based electrolytes in lithium-ion batteries, Journal of Power Sources 542 (2022) 231792.

[28] C. Sang, K. Le, K. Chen, Q. Luo, H. Li, Y. Fang, X. Ai, Temperature-switchable electrolyte with desirable phase transition behavior for thermal protection of lithium-ion batteries, Materials Science and Engineering: R: Reports 163 (2025) 100947.

[29] H. Jiang, X. Han, X. Du, Z. Chen, C. Lu, X. Li, H. Zhang, J. Zhao, P. Han, G. Cui, A PF_6^--permselective polymer electrolyte with anion solvation regulation enabling long-cycle dual-ion battery, Advanced Materials 34 (2022) 2108665.

[30] P. Matteo, T. Akiko, A. Henry, N. Maria Assunta, P. Stefano, Ionic liquids and their derivatives for lithium batteries: role, design strategy, and perspectives, Energy Materials 3 (2023) 300049.

[31] J. Li, J. Chen, X. Xu, J. Shen, Z. Wang, Z. Guo, P. Lin, J. Sun, B. Huang, T. Zhao, Developing quasi-solid-state ether-based electrolytes with trifluorotoluylation ionic liquids for high voltage lithium metal batteries, Advanced Materials 37 (2025) 2501006.

[32] G. Huang, Y. Liao, X. Zhao, X. Jin, Z. Zhu, M. Guan, Y. Li, Tuning a solvation structure of lithium ions coordinated with nitrate anions through ionic liquid-based solvent for highly stable lithium metal batteries, Advanced Functional Materials 33 (2023) 2211364.

[33] S. Li, H. Hong, D. Li, X. Yang, S. Wang, D. Zhang, Q. Xiong, Z. Huang, C. Zhi, Designing zwitterionic bottlebrush polymers to enable long-cycling quasi-solid-state lithium metal batteries, Angewandte Chemie International Edition 64 (2025) e202409500.

[34] Y. Zhang, J. Huang, H. Liu, W. Kou, Y. Dai, W. Dang, W. Wu, J. Wang, Y. Fu, Z. Jiang, Lamellar ionic liquid composite electrolyte for wide-temperature solid-state lithium-metal battery, Advanced Energy Materials 13 (2023) 2300156.

[35] K. Li, A. Hu, R. Xu, W. Xu, B. Yang, T. Li, Y. Li, Z. W. Seh, J. Long, S. Chen, Decoupled ion transport via triadic molecular synergy in flame-retardant quasi-solid electrolytes for safe lithium metal batteries, Advanced Energy Materials 15 (2025) 2501236.

[36] C. Weng, M. Qiu, B. Wang, J. Yang, W. Mai, L. Pan, S. Huang, J. Li, Salt anion's donor number strategy achieving stable NCM622 cathode at 4.7 V, Advanced Functional Materials 35 (2025) 2503438.

[37] C. Weng, M. Qiu, B. Wang, J. Yang, W. Mai, L. Pan, S. Huang, J. Li, Organic cathode electrolyte interphase achieving 4.8 V $LiCoO_2$, Angewandte Chemie International Edition 64 (2025) e202419539.

[38] Y. Yu, S. Qin, Z. Wang, M. Kui, D. Cheng, Y. Xiao, Y. Ren, S. Zhang, J. Chen, X. Xia, W. Hu, H. Yang, Synergistic enhancement effect of G4 and sn in gel polymer electrolyte reinforced by pet nonwoven for lithium metal batteries, Nano Energy 133 (2025) 110454.

[39] X. Jiang, Z. Liu, W. Liu, D. Yu, J. Zhang, X. Wang, Y. Zhang, S. Zhang, Physical ionogels with only 2 wt% gelators as efficient quasi-solid-state electrolytes for lithium batteries, Matter 7 (2024) 1558-1574.

[40] Z. Tian, L. Hou, D. Feng, Y. Jiao, P. Wu, Modulating the coordination environment of lithium bonds for high performance polymer electrolyte batteries, ACS Nano 17 (2023) 3786-3796.

[41] C. Guo, K. Du, R. Tao, Y. Guo, S. Yao, J. Wang, D. Wang, J. Liang, S.Y. Lu, Inorganic filler enhanced formation of stable inorganic-rich solid electrolyte interphase for high performance lithium metal batteries, Advanced Functional Materials 33 (2023) 2301111.

[42] X. Li, Z. Li, W. Zhang, X. Jiang, L. Han, X. Wang, Y. Kan, L. Song, Y. Hu, Flame-retardant in-situ formed gel polymer electrolyte with different valance states of phosphorus structures for high-performance and fire-safety lithium-ion batteries, Chemical Engineering Journal 490 (2024) 151568.

[43] P. Wang, H. Li, N. Li, J. Sun, F. Xu, X. Tian, X. Shi, Electrospinning fiber membrane-derived gel polymer electrolytes with high mechanical strength and low swelling effect for high-safety lithium metal batteries, Advanced Functional Materials 35 (2025) 2413544.

[44] Z. Wang, P. Heasman, J. Rostami, T. Benselfelt, M. Linares, H. Li, A. Iakunkov, F. Sellman, R. Östmans, M. M. Hamedi, I. Zozoulenko, L. Wågberg, Dynamic networks of cellulose nanofibrils enable highly conductive and strong polymer gel electrolytes for lithium-ion batteries, Advanced Functional Materials 33 (2023) 2212806.

[45] S. Zhang, W. Chen, W. Hao, D. Li, C. Zhang, F. Yu, Y. Chen, A composite gel polymer electrolyte by incorporating modified poss endowing inorganic-rich SEI formation and stable cycle life for lithium metal batteries, Chemical Engineering Journal 484 (2024) 149499.

[46] M. Zhou, W. Chen, H. Yang, Y. Hu, T. Lei, D. Chen, S. Wang, Y. Zhang, J. Xiong, Molecular crowding solid polymer electrolytes for lithium metal battery by in situ polymerization, Advanced Energy Materials 15 (2025) 2403082.

Declaration of Competing Interest

The authors declare that they have no known competing financial interests or personal relationships that could have appeared to influence the work reported in this paper.